Acta Oceanol. Sin., 2020, Vol. 39, No. 7, P. 91–106
https://doi.org/10.1007/s13131-020-1603-3
http://www.hyxb.org.cn
E-mail: hyxbe@263.net

Generation and propagation of 21-day bottom pressure variability driven by wind stress curl in the East China Sea

Hua Zheng[1], Xiao-Hua Zhu[1, 2, 3*], Hirohiko Nakamura[4], Jae-Hun Park[5], Chanhyung Jeon[6], Ruixiang Zhao[1], Ayako Nishina[4], Chuanzheng Zhang[1], Hanna Na[7], Ze-Nan Zhu[1], Hong-Sik Min[8]

[1] State Key Laboratory of Satellite Ocean Environment Dynamics, Second Institute of Oceanography, Ministry of Natural Resources, Hangzhou 310012, China

[2] School of Oceanography, Shanghai Jiao Tong University, Shanghai 200030, China

[3] Southern Marine Science and Engineering Guangdong Laboratory (Zhuhai), Zhuhai 519082, China

[4] Faculty of Fisheries, Kagoshima University, Kagoshima 8900056, Japan

[5] Department of Ocean Sciences, Inha University, Incheon 22212, Korea

[6] Department of Mechanical Engineering, Massachusetts Institute of Technology, Cambridge 02139, USA

[7] School of Earth and Environmental Sciences, Seoul National University, Seoul 08826, Korea

[8] Ocean Circulation and Climate Research Center, Korea Institute of Ocean Science and Technology, Busan 49111, Korea

Received 6 March 2020; accepted 15 April 2020

Abstract

Between June 2015 and June 2017, two pressure-recording inverted echo sounders (PIESs) and five current and pressure-recording inverted echo sounders (CPIESs) deployed along a section across the Kerama Gap acquired a dataset of ocean bottom pressure records in which there was significant 21-day variability (P_{bot21}). The P_{bot21}, which was particularly strong from July–December 2016, was coherent with wind stress curl (WSC) on the continental shelf of the East China Sea (ECS) with a squared coherence of 0.65 for a 3-day time lag. A barotropic ocean model demonstrated the generation, propagation, and dissipation of P_{bot21}. The modeled results show that the P_{bot21} driven by coastal ocean WSC in the ECS propagated toward the Ryukyu Island Chain (RIC), while deep ocean WSC could not induce such variability. On the continental shelf, the P_{bot21} was generated nearly synchronously with the WSC from the coastline to the southeast but dissipated within a few days due to the effect of bottom friction. The detection of P_{bot21} by the moored array was dependent on the 21-day WSC patterns on the continental shelf. The P_{bot21} driven southeast of the Changjiang Estuary by the WSC was detected while the P_{bot21} generated northeast of the Changjiang Estuary was not.

Key words: pressure-recording inverted echo sounder, East China Sea, bottom pressure, wind stress curl

Citation: Zheng Hua, Zhu Xiao-Hua, Nakamura Hirohiko, Park Jae-Hun, Jeon Chanhyung, Zhao Ruixiang, Nishina Ayako, Zhang Chuanzheng, Na Hanna, Zhu Ze-Nan, Min Hong-Sik. 2020. Generation and propagation of 21-day bottom pressure variability driven by wind stress curl in the East China Sea. Acta Oceanologica Sinica, 39(7): 91–106, doi: 10.1007/s13131-020-1603-3

1 Introduction

Ocean bottom pressure (P_{bot}), the vertical integral of atmospheric and oceanic mass, is a fundamental quantity in oceanography. Understanding of P_{bot} contributes to determining changes in ocean circulation, heat content, and sea level rise (Ponte et al., 2007). However, compared with ocean temperature, salinity, and currents, knowledge of P_{bot} remains poor due to the sparseness of observations in time and space.

Since 2002, owing to the Gravity Recovery and Climate Experiment (GRACE) mission, global P_{bot} can be observed at monthly intervals by satellites. However, the captured frequencies of the signals are restricted by the 60-day Nyquist period resulting from the coarse temporal resolution (Na et al., 2012; Quinn and Ponte, 2011). Furthermore, the accuracy of the GRACE is limited by non-negligible aliasing errors (Gille and Hughes, 2001). The Ocean Model for Circulation and Tides (OMCT) or the Estimating the Circulation and Climate of the Ocean (ECCO) project have been applied for de-aliasing of P_{bot} records in GRACE; however, despite this, the aliasing errors of high-frequency (< 60 days) P_{bot} remain severely underestimated (Quinn and Ponte,

Foundation item: The SIO group was supported by the National Natural Science Foundation of China under contract Nos 41920104006, 41806020, 41776107 and 41906024; the National Programme on Global Change and Air–Sea Interaction under contract No. GASIIPOVAI-01–02; the Scientific Research Fund of SIO under contract Nos JZ2001 and JT1801; the Project of State Key Laboratory of Satellite Ocean Environment Dynamics, SIO under contract Nos SOEDZZ1901 and SOEDZZ1903; the Kagoshima University group was supported by Core Research for Evolutional Science and Technology of the Japan Science and Technology Corporation and by JSPS KAKENHI under contract Nos JP15H05821 and JP15H03725; Jae-Hun Park, Hanna Na and Hong-Sik Min were supported by the "Study on Air–Sea Interaction and Process of Rapidly Intensifying Typhoon in the Northwestern Pacific" project funded by the Ministry of Oceans and Fisheries, Korea.
*Corresponding author, E-mail: xhzhu@sio.org.cn

2011). In addition, sea surface height changes measured by TOPEX/Poseidon (T/P) and Jason-1/2/3 includes steric and mass-loading components; the former is associated with subsurface temperature and salinity changes, and dominates low-frequency variabilities; the latter is associated with P_{bot} and is more important for high-frequency variabilities (Fukumori et al., 1998; Park et al., 2008, 2012). Sea surface height products from satellites are aliased or distorted at high-frequency bands due to the coarse temporal resolution (Park et al., 2012). P_{bot} could be measured by different kinds of marine instruments such as CTD and glider (Qiu et al., 2019), but most of them only provide discontinuous records, to avoid aliasing errors and improve our understanding of high-frequency P_{bot}, *in situ* observations are necessary. Accurate and precise sensors are required for deployment in the ocean, because subtidal dynamic pressure can be less than 8 hPa, while ambient pressures are always more than 10^5 hPa (Watts et al., 2001).

Brown et al. (1975) used measured data to study ocean bottom pressure in 1975, and since then, P_{bot} with different periods has been observed in many areas. Based on long-term and high-frequency P_{bot} records measured during the North Pacific Barotropic Electromagnetic and Pressure Experiment (BEMPEX), P_{bot} variability at time scales longer than 10 days was found to be driven by large-scale atmospheric forcing (Luther et al., 1990). In the Japan/East Sea, P_{bot} variability with periods of 2–7 days driven by atmospheric pressure has been observed (Park and Watts, 2005). Park and Watts (2006) indicated that non-isostatic P_{bot} variability at a near 5-day period is related to global Rossby–Haurwitz waves, which have been reported by numerical modeling studies (Carrère and Lyard, 2003; Mathers and Woodworth, 2004; Ponte, 1997). In the Kuroshio Extension System Study (KESS), near 13-day P_{bot} variability to the east of Japan was found to be driven by large-scale wind stress curl (WSC) in the North Pacific (Na et al., 2012). In the South China Sea, P_{bot} variability with a period of near 5 days results from the combination of Rossby–Haurwitz waves and coastal-trapped waves (Zhao et al., 2017), and a P_{bot} response with a near 7-day period is closely related to local atmospheric surface pressure (SP) and wind-forced Ekman pumping/suction (Zhang et al., 2018).

P_{bot} variability is directly affected by the change of sea surface height, which shows significant coherence with wind stress curl (Fu, 2003; Fu and Davidson, 1995). Na et al. (2016) suggested that winds become increasingly important in driving P_{bot} variability as the period decreases from 60 to 7 days. According to Luther et al. (1990) and Na et al. (2012), local WSC can be crucial for variability of P_{bot} with periods shorter than 10 days. For periods longer than 10 days, P_{bot} variability was observed to be driven by non-local WSC in the North Pacific. Nevertheless, few studies have reported P_{bot} variability with periods longer than 10 days driven by WSC in shallow marginal seas.

In East Asia, observations of P_{bot} have been recorded in the South China Sea, Japan/East Sea, and North Pacific, but knowledge of P_{bot} in the East China Sea (ECS) remains limited. The ECS is characterized by a broad continental shelf and a steep slope on the shelf edge, and is separated from the North Pacific by the Ryukyu Island Chain (RIC). The Kuroshio Current lies to the west of the RIC (Nitani, 1972) and the Ryukyu Current to the east of the RIC (Zhu et al., 2003; Wang et al., 2019). As a part of the Joint Kuroshio–Ryukyu Current System Study (JKRYCSS), two pressure-recording inverted echo sounders (PIESs) and five current and pressure-recording inverted echo sounders (CPIESs) were deployed along a section transecting the Kuroshio and Ryukyu currents near Miyakojima Island, southwest of the Kerama Gap, the deepest channel connecting the ECS to the North Pacific in the RIC. Pressure sensors on the PIESs/CPIESs provided 2-year *in situ* P_{bot} records, and provide the opportunity to investigate the P_{bot} variability. Based on this project, poleward-propagating near-inertial waves enabled by the western boundary current were observed (Jeon et al., 2019). P_{bot} variability describes the barotropic information of the western boundary current here, it is especially important for the Ryukyu Current, which is characterized by a strong subsurface velocity core that we have analyzed in another study (Zhao et al., 2020). In this study, we focused on the WSC-driven P_{bot} variability with a period of 21-day; such variability cannot be observed by GRACE due to the monthly sample interval. Variability with such a period is ubiquitous in the atmosphere around East Asia. Previous studies have identified wind-driven rainfall with periods including 21 days around the Changjiang River Basin (Chen et al., 2000; Mao and Wu, 2006; Yang et al., 2010). However, few studies have concentrated on how atmosphere forcing influences the ocean at this period.

The paper is organized as follows. The data and processing methods used in the study are described in Section 2. Section 3 describes the P_{bot} records from the observations, and a barotropic model is used to investigate the detailed relationship with WSC and propagation characteristics. A summary is given in Section 4.

2 Data and methods

2.1 *Data*

With the aim of clarifying the temporal and spatial evolution of the Kuroshio and Ryukyu currents and their interactions, the JKRYCSS mission was carried out from June 2015 to June 2017 by the Second Institute of Oceanography, Ministry of Natural Resources, China; Kagoshima University, Japan; the Korea Institute of Ocean Science and Technology; and Inha University, Korea. Multiple observation methods, including seven PIESs/CPIESs, were applied along the TOPEX/Poseidon and Jason-1/2/3 satellite altimeter track (Pass 62) to observe the Kuroshio and Ryukyu currents southwest of the Kerama Gap near Miyakojima Island (Fig. 1).

As a part of the JKRYCSS, two PIESs and five CPIESs were arrayed in this section for approximately 2 years (Fig. 1 and Table 1). Three (KES1, KES2, KES3) were on the west side of the RIC (the Kuroshio Current side, in the ECS), and four (RES1, RES2, RES3, RES4) were on the east side (the Ryukyu Current side, in the North Pacific). KES1 and KES3 each comprised a PIES, an echo sounder that rests on the seafloor and records acoustic round-trip travel time, bottom pressure, and bottom temperature. Other sites utilized CPIESs, which are equipped with Aanderaa Doppler Current Sensors positioned about 50 m above the PIES for near-bottom current measurement. A pressure sensor with a resolution of 0.001×10^4 Pa, absolute accuracy of ± 0.01% and full-scale range of $6\ 000\times10^4$ Pa equipped on each PIES/CPIES provided high-resolution P_{bot} records with a 10-min temporal interval (Inverted Echo Sounder User Manual, http://www.po.gso.uri.edu/dynamics/IES/index.html). Following the procedures proposed by Kennelly et al. (2007), time series of P_{bot} (Fig. 2a) were despiked, detided, and dedrifted. The P_{bot} records were resampled with a one-hour interval, and the times of records were converted to Coordinated Universal Time (UTC). Statistically significant peaks at a period of 21-day can be seen in the variance-preserving spectra for the P_{bot} records (Fig. 2b). In this study, in order to focus on the 21-day-period variability, a third-order Butterworth filter with cut-off periods of 19.5 and 22.5 days was ap-

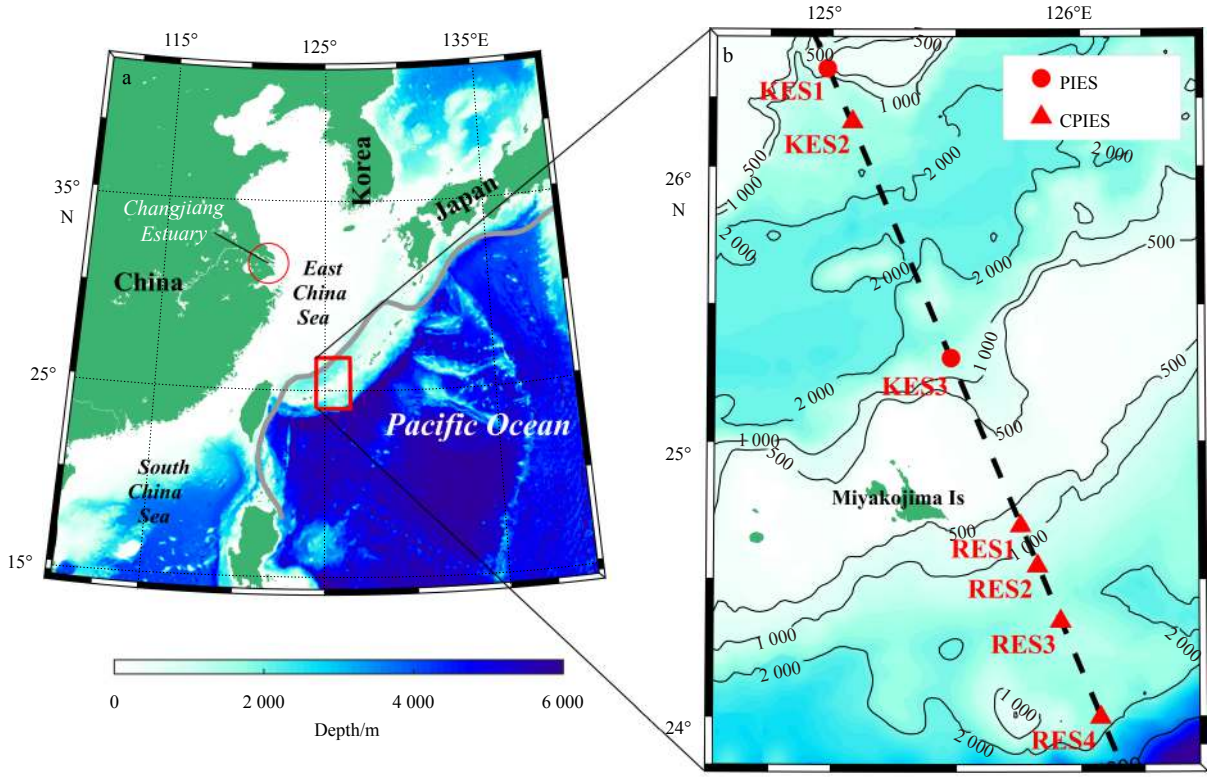

Fig. 1. Map of the study region (a) and pressure-recording inverted echo sounder (PIESs; red dots) and current and pressure-recording inverted echo sounder (CPIESs; red triangles) positions along the Jason-class satellite altimeter track (black dashed line) (b). Colors and black contours show bathymetry in meters. The path of the Kuroshio Current is indicated by gray line in (a).

Table 1. Position and depth of each PIES/CPIES site

Station	PIES/CPIES	North latitude	East longitude	Depth/m
KES1	PIES	26°21.42′	124°58.74′	588
KES2	CPIES	26°09.78′	125°04.86′	1 520
KES3	PIES	25°18.30′	125°28.74′	1 414
RES1	CPIES	24°41.64′	125°45.48′	720
RES2	CPIES	24°32.88′	125°59.50′	1 191
RES3	CPIES	24°20.82′	125°55.02′	1 979
RES4	CPIES	23°59.88′	126°04.56′	1 677

plied to $P_{\rm bot}$ records.

The variance of a signal is equal to the signal power with its mean subtracted. Statistically significant and dominant periodicities of $P_{\rm bot}$ records were identified by variance-preserving spectra using the periodogram method. Before computation, the series were high pass filtered with period of 90 days to focus on the intraseasonal variability, 5% of the series on each end were tapered using split cosine bell window. The periodogram was smoothed over three adjacent frequencies with modified Daniell window; there were 5.05 degrees of freedom. The variance-preserving spectra were plotted as the power times the frequency (Thomson and Emery, 2001). Whether the spectral is statistically significant is based on the spectrum of Markov red noise following the method of Gilman et al. (1963). Complex empirical orthogonal function (CEOF) analysis (Barnett, 1984) was used to describe the spatial pattern and propagation of the 21-day $P_{\rm bot}$ variability.

Six-hourly 10-m wind and SP data from the National Centers for Environmental Prediction/National Centers for Atmospheric Research (NCEP/NCAR) reanalysis (https://www.esrl.noaa.gov/psd/data/gridded/data.ncep.reanalysis.html; Kalnay et al., 1996) were used to determine the relationship between $P_{\rm bot}$ and atmospheric forcing. The spatial resolutions of the wind and SP data were 1.905° latitude × 1.875° longitude and 2.5° latitude × 2.5° longitude, respectively. To illustrate that the 21-day signal is not influenced by small-scale noise in the NCEP/NCAR products, products from European Center for Medium-range Weather Forecasts reanalysis (ERA-interim) (https://apps.ecmwf.int/datasets/) and Japanese 55-year Reanalysis datasets (JRA-55) (https://jra.kishou.go.jp/JRA-55) were also used for comparison. Wind stress was calculated from wind records, as follows:

$$\tau = \rho_{\rm a} C_D U_{10}^2, \tag{1}$$

where $\rho_{\rm a}$ is the density of air, C_D is the drag coefficient, and U_{10} is the wind speed at 10 m. The C_D used here was determined by Trenberth et al. (1990). The WSC was calculated based on wind stress from the NCEP/NCAR, ERA-interim, and JRA-55 products.

The Ekman pumping/suction velocity (upward positive, $w_{\rm E}$), which is the vertical velocity at the base of the Ekman layer, was calculated as follows (Talley et al., 2011):

$$\frac{\partial U_{\rm E}}{\partial x} + \frac{\partial V_{\rm E}}{\partial y} = \nabla \cdot \vec{U}_{\rm E} = -(w_{\rm surface} - w_{\rm E}) = w_{\rm E}, \tag{2}$$

where the vertical velocity at the surface in steady state $w_{\rm surface} = 0$, $U_{\rm E}$ and $V_{\rm E}$ are eastward and northward Ekman transport components, respectively. $\nabla \cdot \vec{U}_{\rm E}$ was calculated by taking the curl of the linear, steady, vertically-integrated, horizontal momentum equations:

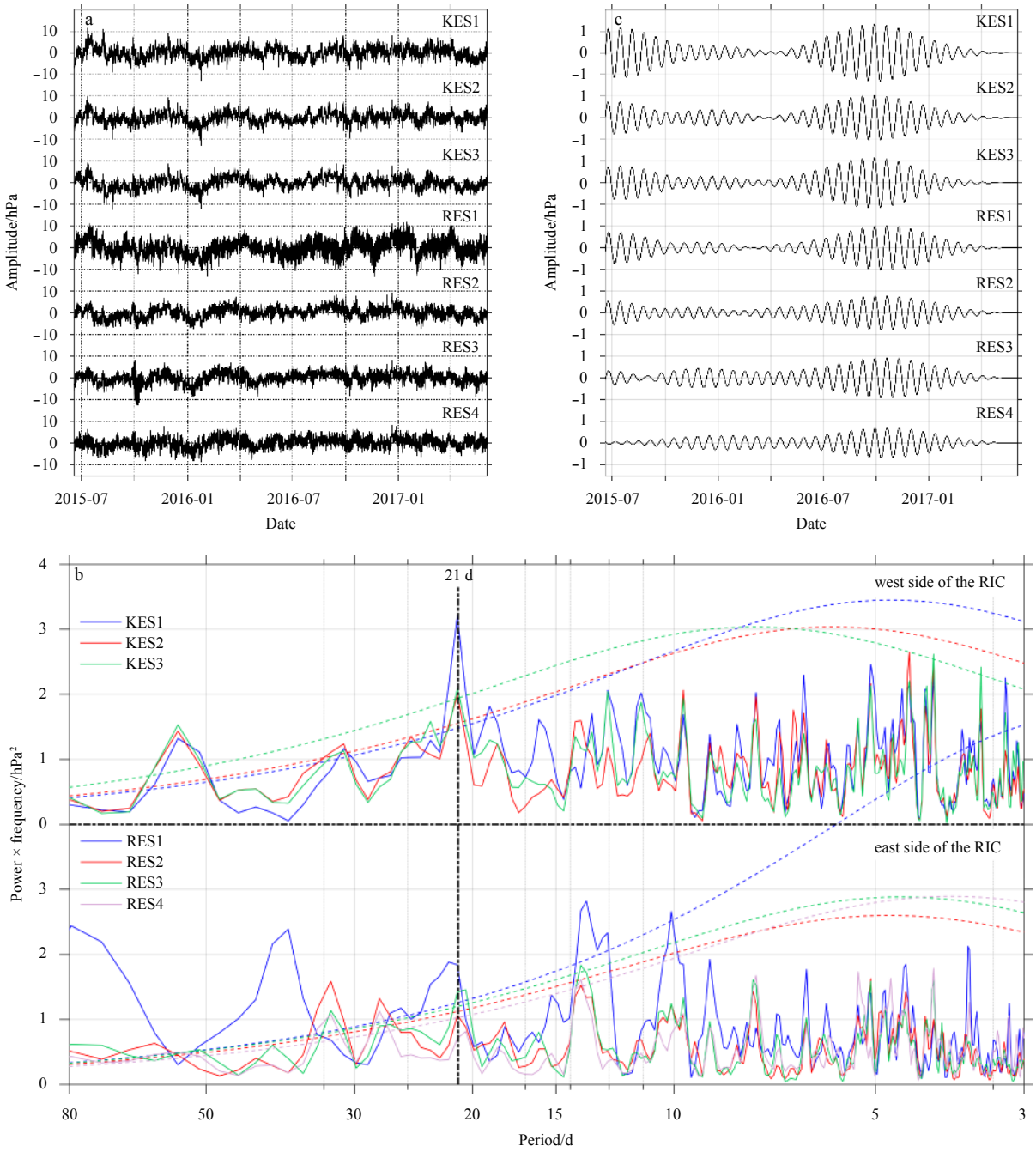

Fig. 2. Time series of measured ocean bottom pressure (P_{bot}) variability (a), P_{bot} variance-preserving spectra (b) and time series of band-pass-filtered (19.5–22.5 d) P_{bot} (c). The 95% confidence level of red noise (the colored dashed lines) and 21-day period (the black vertical line) are indicated.

$$\nabla \cdot \vec{U}_E = \vec{k} \cdot \nabla \times \frac{\vec{\tau}}{\rho f}, \tag{3}$$

where $\vec{k}$ is the vertical unit vector, $\vec{\tau}$ is the wind stress, ρ is seawater density, and f is the Coriolis parameter. The WSC and w_E were also band-pass filtered with a third-order Butterworth filter with cut-off periods of 19.5 and 22.5 days.

2.2 *Barotropic model*

To compensate for the spatial distributions of P_{bot} records and to explore possible mechanisms for this, the free-surface, terrain-following, primitive-equation Regional Ocean Modeled System (ROMS; http://www.myroms.org) (http://www.myroms.org) was used to simulate the variability of P_{bot} in the ECS and around the moored array (the red box in Fig. 1a). The bottom topography in the model is based on the Earth topography five minute grid (ETOPO5; https://www.ngdc.noaa.gov/mgg/global/etopo5.HTML). The ROMS model covers the region from 100° E to 70°W and 35°S to 65°N with a spatial resolution of (1/12)°. The temporal interval of the model output is 1 day. The vertically integrated momentum equation is solved by the barotropic component; variations in density are ignored. The ROMS eastern boundary at 70° W is closed whereas the southern, northern, and western boundaries are open based on the Flather boundary

condition for barotropic normal velocity components (Flather, 1976). Moreover, a free-surface gradient condition is applied to the surface elevation at the open boundaries by setting them as the closest interior value.

The ROMS model used only wind stress forcing. Although atmospheric forcing includes SP and wind could induce variability in the ocean, the influence of SP becomes more important than that of wind only at periods of shorter than approximately three days (Ponte, 1994). Hirose et al. (2001) found that modeled results from the barotropic shallow water model are similar when considering wind forcing alone and when considering both wind and pressure forcing. In addition, SP did not show significant 21-day variability (see Section 3.1). Therefore, the wind stress product from NCEP/NCAR was considered as the only forcing in the model. The model was run from January 1, 2015 to December 31, 2017, covering the observation period. Additional experiments were run during 2016 with a flat bottom over the ECS at depths of 50, 100, 300, 500, 700, and 1 000 m. These experiments helped to distinguish the effect of ocean depth on 21-day P_{bot} variability. Modeled results were also band-pass filtered by the same Butterworth filter applied to observed records.

3 Results

3.1 *Observed 21-day ocean bottom pressure variability*

The seven PIESs/CPIESs with high-resolution pressure sensors arrayed near Miyakojima Island provide 2-year P_{bot} records with a maximum amplitude of approximately 10 hPa (Fig. 2a). Figure 2b shows that statistically significant P_{bot} peaks at period of 21 days can be found at each site from variance-preserving spectra. Generally speaking, the P_{bot21} weakens from west to east, and 21-day peak at RES4 did not reach the 95% confidence level of red noise. The P_{bot21} at RES2–4 was much weaker than that west of the RIC (KES1-3), while the energy of the P_{bot21} at the site closest to the RIC (RES1) approached the energy at KES2 and KES3.

To obtain a more complete understanding of the temporal variability of the P_{bot21} around the mooring sites, band-pass-filtered P_{bot} records from the third-order Butterworth filter with cut-off periods of 19.5 and 22.5 d are shown in Fig. 2c. The band-pass-filtered records on the west side of RIC were more energetic than the east side. All seven sites showed nearly in-phase variability with high amplitude of approximately 1 hPa from July to December 2016. However, as expected, the CPIES-measured near-bottom current velocity, which are more sensitive to local bottom variabilities as compared with bottom pressure (Niiler et al., 1993), did not have any statistically significant variability at a 21-day period in either the zonal (u) or meridional (v) component.

According to previous studies, atmospheric forcing, including SP and wind, can be vital to P_{bot} (Luther et al., 1990; Park and Watts, 2006; Zhang et al., 2018). Multiple and partial coherences analysis was used to separately identify the contribution of SP and WSC as well as the mutual coherences between them. For simplicity, we use 7-site averaged ocean bottom pressure ($aveP_{bot}$) here. The P_{bot21} was not coherent with local SP and WSC around the mooring sites because the coherences were all below the 95% confidence level (Fig. 3a). Figure 3b shows an obvious peak of multiple coherence with a 21-day period on the continental shelf of the ECS, and WSC dominated the P_{bot21} rather than SP, which did not reach the 95% confidence level for this period. The SP becomes less important and wind-driven variability dominates at periods longer than approximately 3 days (Ponte, 1994). Therefore, only the WSC was considered in further analyses.

The 21-day-period variability in SP was not statistically significant, both around the moored array (Fig. 4a) and on the continental shelf of the ECS (Fig. 4b). Obvious 21-day signals were found in the WSC around the moored array (Fig. 4c) and on the continental shelf of the ECS (Fig. 4d). The ERA-interim data set (magenta lines) and JRA-55 data set (cyan lines) also show simil-

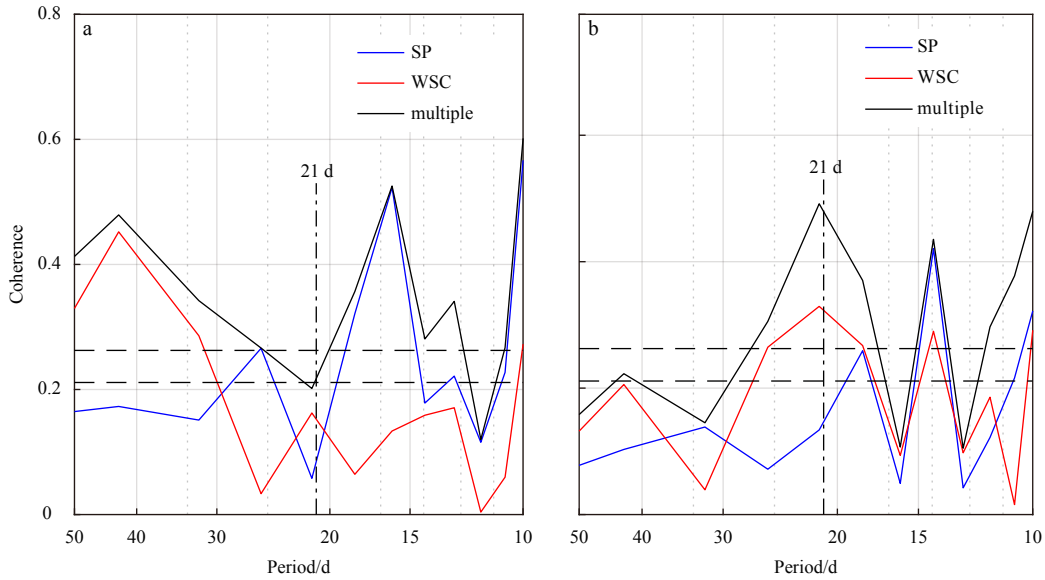

Fig. 3. Multiple (black lines) and partial (blue and red lines) coherences between output ($aveP_{bot}$) and two inputs (SP and WSC) for spatially averaged surface pressure (SP) and wind stress curl (WSC) around the moored array (a) and spatially averaged SP and WSC on the continental shelf of the East China Sea (ECS) (b). The 95% confidence level (horizontal lines, 0.26 for multiple coherence and 0.21 for partial coherences) and 21-day period (vertical line) are also indicated. "Spatially averaged" means the average of variable in a given range, which is distinct from "temporally averaged". The continental shelf of the ECS in this paper indicates the region south of 35.5°N in the ECS with depth less than 200 m.

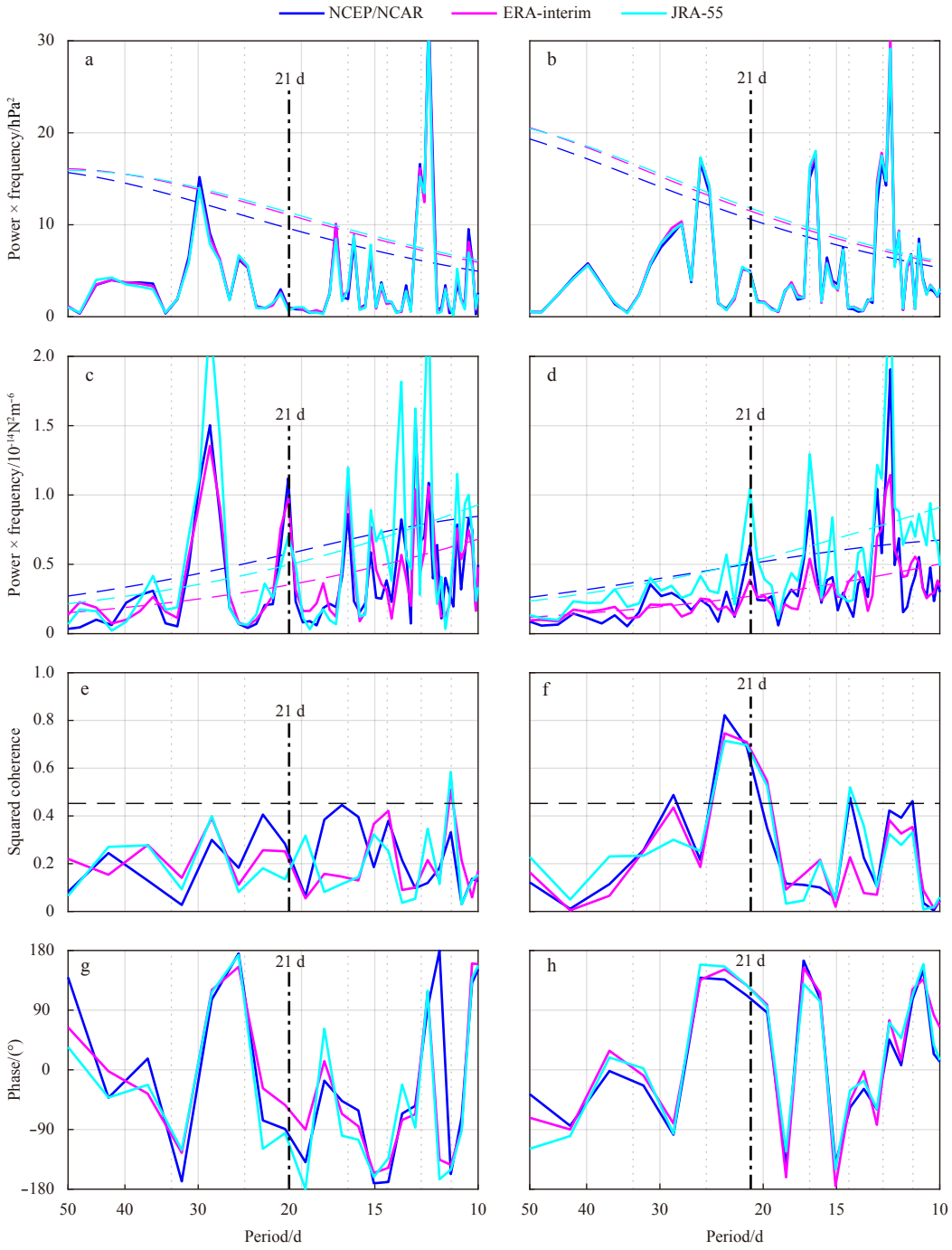

Fig. 4. Mean variance-preserving spectra of surface pressure (SP) (a, b) and wind stress curl (WSC) (c, d) around the moored array (left) and on the continental shelf of the East China Sea (ECS) (right). Squared coherence (e, f) and phase (g, h) between seven-site averaged P_{bot} ($aveP_{bot}$) and spatially averaged WSC around the moored array (left) and on the continental shelf of the ECS (right). NCEP/NCAR, ERA-interim, and JRA-55 data are shown. SP and WSC are 5-day smoothed. The 95% confidence level (horizontal lines) and 21-day period (vertical lines) are indicated.

ar signals from SP and wind, which suggests that this is not an artifact from the NCEP/NCAR products. The P_{bot21} was significantly coherent with the WSC on continental shelf (with a squared coherence of 0.65, Fig. 4f) but not with that around the moored array (Fig. 4e), which indicates that the signal might be from the northwest. The WSC affects P_{bot} through Ekman divergence/convergence; ocean mass convergence (divergence) occurs when the WSC is negative (positive), which results in increasing (decreasing) P_{bot} (Na et al., 2012; Wang et al., 2011). Figure 4h shows that the mean phase between P_{bot21} at KES1 and WSC on the continental shelf was approximately –125°; considering the negative correlation between P_{bot} and WSC, the 21-day WSC lead P_{bot21} at KES1 of approximately 55° (~3 days).

3.2 *Modeled 21-day ocean bottom pressure variability*

Barotropic ROMS model results were used to investigate the

mechanisms of P_{bot21} generation and propagation. Figure 5 shows a comparison of modeled P_{bot} records around the moored array (red box in Fig. 1a) with observed $aveP_{bot}$ records. The normalized raw data from observations and from ROMS show similar variability (Fig. 5a). The normalized 21-day band-pass-filtered records are almost in-phase with a coherence of 0.82, especially at high-amplitude times (Fig. 5b). The modeled P_{bot21} showed a maximum amplitude in September 2016, but almost disappeared from October 2015 to March 2016, which is consistent with the observations.

To investigate propagation among mooring sites, Figs 5c and d show the Hovmöller diagrams of the P_{bot21} during the period with highest amplitude (9–29 September 2016). The model speed component along the PIES section from KES1 to RES4 was approximately 2.0 m/s, which is close to the observed 2.4 m/s. The observed P_{bot21} signal became weaker when propagating from the west of the RIC to the east. However, the observed results show that the amplitude was lower at RES2 than at other sites and that the phase was behind the others (Fig. 5c). This result might be due to the influence of the RIC. In addition, the wind-only forced barotropic model matched the observations well, especially during the high amplitude period, and is reliable for use in further analysis.

Figure 6 shows the variance-preserving spectra of the modeled P_{bot} and the time series of the modeled P_{bot21} around the array and on the continental shelf. As with the observations, modeled results show a significant high-amplitude 21-day signal from July to December 2016 around the moored array (Figs 6a and b). The modeled P_{bot} in the ECS showed a higher-energy 21-day signal (Fig. 6c), but high-amplitude could also be found from January to June 2016 (Fig. 6d) as compared with the records shown in Fig. 6b. Figures 6a and c show energetic variability with a period of about 17 days, which corresponds to the 17-day variability in WSC (Figs 4c and d); however, it was not observed from the actual data (Fig. 2b). Variability with the same period was also found in the SP (Figs 4a and b). The mechanism of the 17-day variability may be too complex to be explained by the wind-only forced barotropic model.

To investigate the propagation of P_{bot21}, daily maps of the highest amplitude period (9–29 September 2016) are shown in Fig. 7. During 9–29 September 2016, the 21-day signal had a maximum amplitude of approximately 3 hPa southeast of the Changjiang Estuary on the continental shelf, some 300 km from the mooring sites, with a depth of about 60–80 m. The propaga-

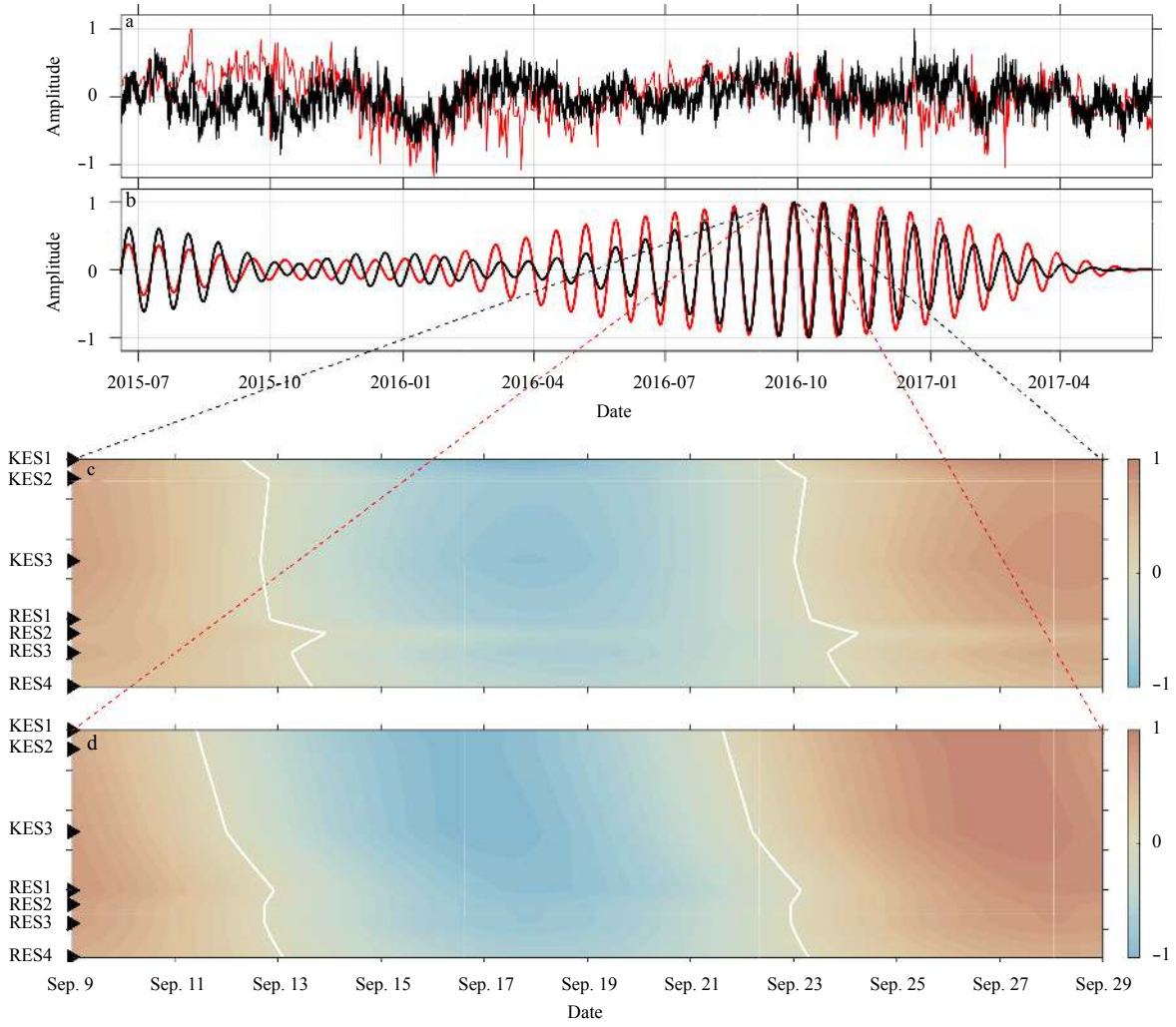

Fig. 5. Comparison of observed $aveP_{bot}$ (black line) and modeled P_{bot} around the moored array (red line). a. Normalized records; b. Normalized band-pass-filtered (19.5–22.5 d) records; c, d. Normalized 21-day Hovmöller diagrams for observed and ROMS records, respectively. White lines represent zero contours.

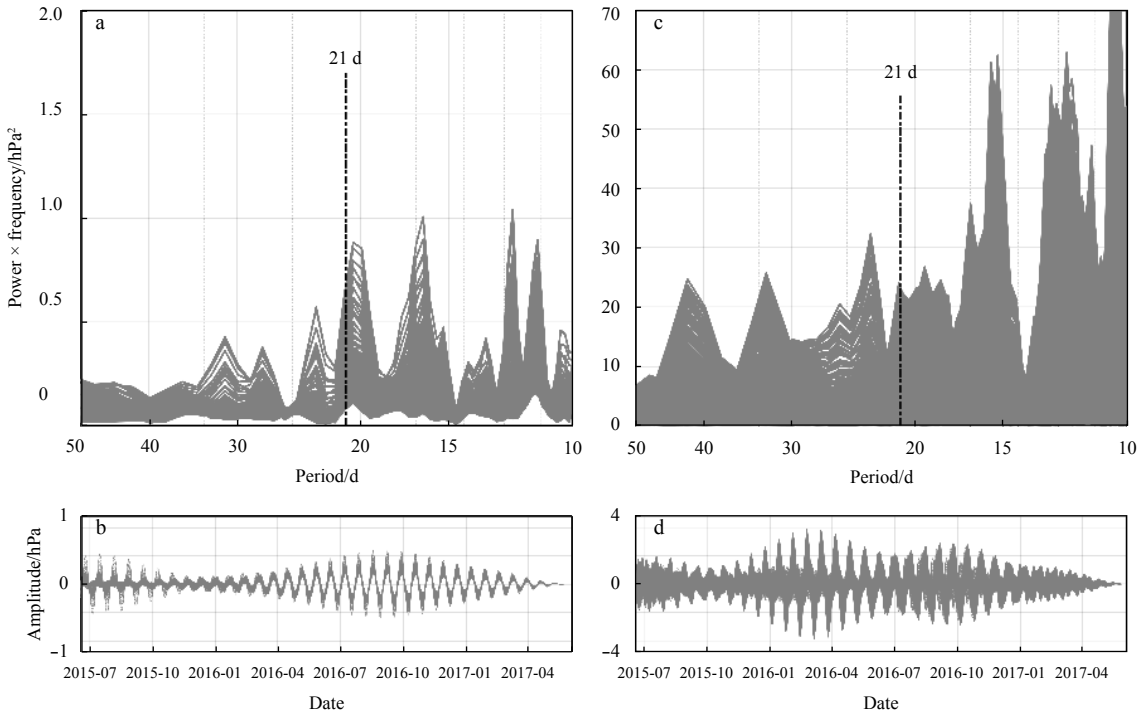

Fig. 6. Variance-preserving spectra of modeled P_{bot} around the moored array (a), band-pass-filtered (19.5–22.5 d) modeled P_{bot} around the moored array, c and d are same as a and b, but for modeled P_{bot} on the continental shelf of the East China Sea. Gray lines are the data from each sampling point. 21-day period (black vertical lines) are indicated.

tion of the signal can be observed clearly from the zero contour lines plotted in Fig. 7. The 21-day variability appeared in the east coast of China with a negative amplitude on September 9; then expanded southeastward perpendicular to the coastline. The negative signal southeast of the Changjiang Estuary lasted for a few days (12–18 September 2016) before the next positive signal arrived. The largest amplitude appeared during 14–16 September. The variability in the coastal area turned positive and expanded southeastward as the negative signal in the ECS became weaker; then the largest amplitude was found southeast of the Changjiang Estuary from 24–27 September. In general, the variability was generated and propagated on continental shelf, but the energy decreased rapidly as the signal expanded from the shelf to the North Pacific as shown in the lower panel (red line). On September 22, the zero contour line was close to KES1, and on September 24 it had reached RES4, taking less than 2 days to propagate between the two, which is consistent with the observations (Fig. 5c).

Figure 8 shows 21-day WSC daily maps with the highest amplitudes for the continental shelf east of the Changjiang Estuary from 9–29 September 2016; these maps are correlated with the highest-amplitude P_{bot21} period, suggesting that the WSC induced the P_{bot21}. As shown in the upper panel of Fig. 8, significant negative correlation was found between the 21-day WSC and the P_{bot21} on the continental shelf. The largest positive signal of the 21-day WSC (the blue line) appeared from 14–16 September and the largest negative signal appeared on September 25, corresponding to the largest negative and positive variabilities of the P_{bot21} (the black line). The phase between the P_{bot21} and the 21-days WSC is ~10° (~0.6 days), which indicates that coastal WSC in the ECS induced the local P_{bot21} through the Ekman divergence/convergence with little time lag. The Ekman divergence/convergence characterized by w_E (the orange line) corresponded to the 21-day WSC and P_{bot21}. The P_{bot21} is much weaker for the region around the moored array than on the continental shelf; it corresponds to the negative and positive maxima of 17–19 September and 27–29 September, respectively (the red line). There is a clear near-3-day time lag between the P_{bot21} around the moored array and both the 21-day WSC and the P_{bot21} on the continental shelf. WSC from NCEP/NCAR (the blue line), ERA-interim (the magenta line), and JRA-55 (the cyan line) show 21-day signals similar to what was indicated in the lower panel. WSC-driven P_{bot21} on the shelf shows a similar spatial pattern as the 21-day WSC there (Figs 7 and 8). It took around 7 days (16–22 September) for the 21-day WSC to propagate from the coast to the 200-m isobaths in the ECS, and the same was observed for the 21-day modeled P_{bot} response. The P_{bot21} generated from coastline to the southeast following the propagation of the 21-day WSC, became weaker due to the decrease of the 21-day WSC (red and blue lines in the lower panel of Fig. 7).

However, the spatial patterns of the P_{bot21} and the 21-day WSC differed significantly in the North Pacific and around the moored array. The P_{bot21} around the mooring array was from the ECS, but the 21-day WSC there seems to come from the Pacific Ocean; as such, local 21-day WSC could not drive the P_{bot21} in this deep region (lower panel of Fig. 7), and the signal there was from the ECS. The P_{bot21} decreased more slowly in deep region compared to on the shelf; the amplitude only decreased from ~0.34 hPa at 125°E to ~0.24 hPa at 126°E (lower panel of Fig. 7). The significant P_{bot21} southeast of the Changjiang Estuary took ~3 days to propagate to the mooring sites.

To examine why the significant P_{bot21} in the ECS in early 2016 did not propagate to the RIC, Fig. 9 shows modeled daily maps of band-pass-filtered (19.5–22.5 d) WSC from 9–29 February 2016. In contrast to the increase near the coast on September 9, variability with a negative amplitude appeared in the northern ECS on

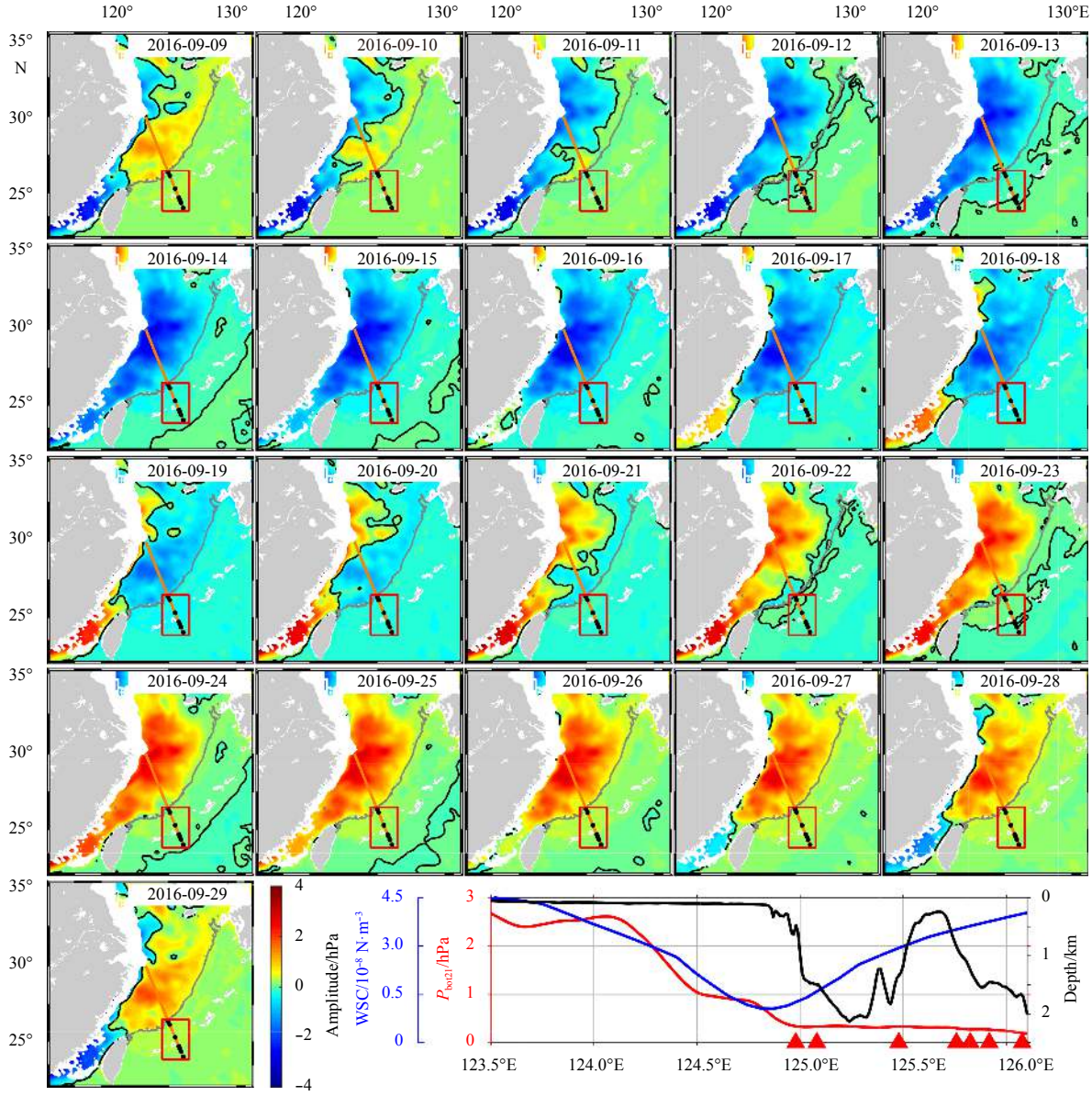

Fig. 7. Daily maps of the modeled 21-day bottom pressure variability (P_{bot21}) from 9–29 September 2016. The colors show P_{bot21} and the black lines are zero contours. Gray lines are 200-m isobaths on the continental shelf of the East China Sea. Black dots indicate pressure-recording inverted echo sounder (PIES)/current and pressure-recording inverted echo sounder (CPIES) sites; the red box indicates the region around the moored array. In the lower right panel, the topography along the orange line across the PIES/CPIES is indicated by a black line. The largest positive value of the modeled P_{bot21} (red line) and WSC (blue line) at each point of the orange line are also indicated. Red triangles are PIES/CPIES locations.

February 9 and then expanded southward, with the largest amplitude occurring east of the Changjiang Estuary on February 14. As the negative signal in the ECS weakened, the northern ECS became positive and the largest positive signal occurred east of the Changjiang Estuary between 24–25 February. However, zero contour lines remained around the mooring sites during this entire period; this means that the 21-day signal had almost disappeared around the mooring sites during February 2016, which is consistent with the measured records. The 21-day signal generated by the WSC covered the entire continental shelf in September 2016, but covered only the area north of 27°N on the shelf in February 2016. The different spatial patterns in these two periods suggest that P_{bot21} could have extended farther south to the mooring sites in September 2016, but that they had dissipated on the shelf in February 2016 after leaving the large 21-day WSC region; the amplitude decreased from ~1.72 hPa at 124°E to ~0.22 hPa at 124.5°E (lower panel of Fig. 9). Although the 21-day WSC increased east of ~124.2°E (the blue line), the P_{bot21} (the red line) did not increase owing to the increasing depth.

During early 2016, the amplitude of P_{bot21} was high in the northern ECS. However, as it could not be measured by the PIESs/CPIESs (Fig. 2c), daily maps of 21-day WSC from 9 to 29 February 2016 were picked out in Fig. 10 to identify the reason. In February 2016, the negative correlation between P_{bot21} and 21-day WSC (w_E) on the continental shelf remained significant. The largest positive and negative signals of 21-day WSC occurred dur-

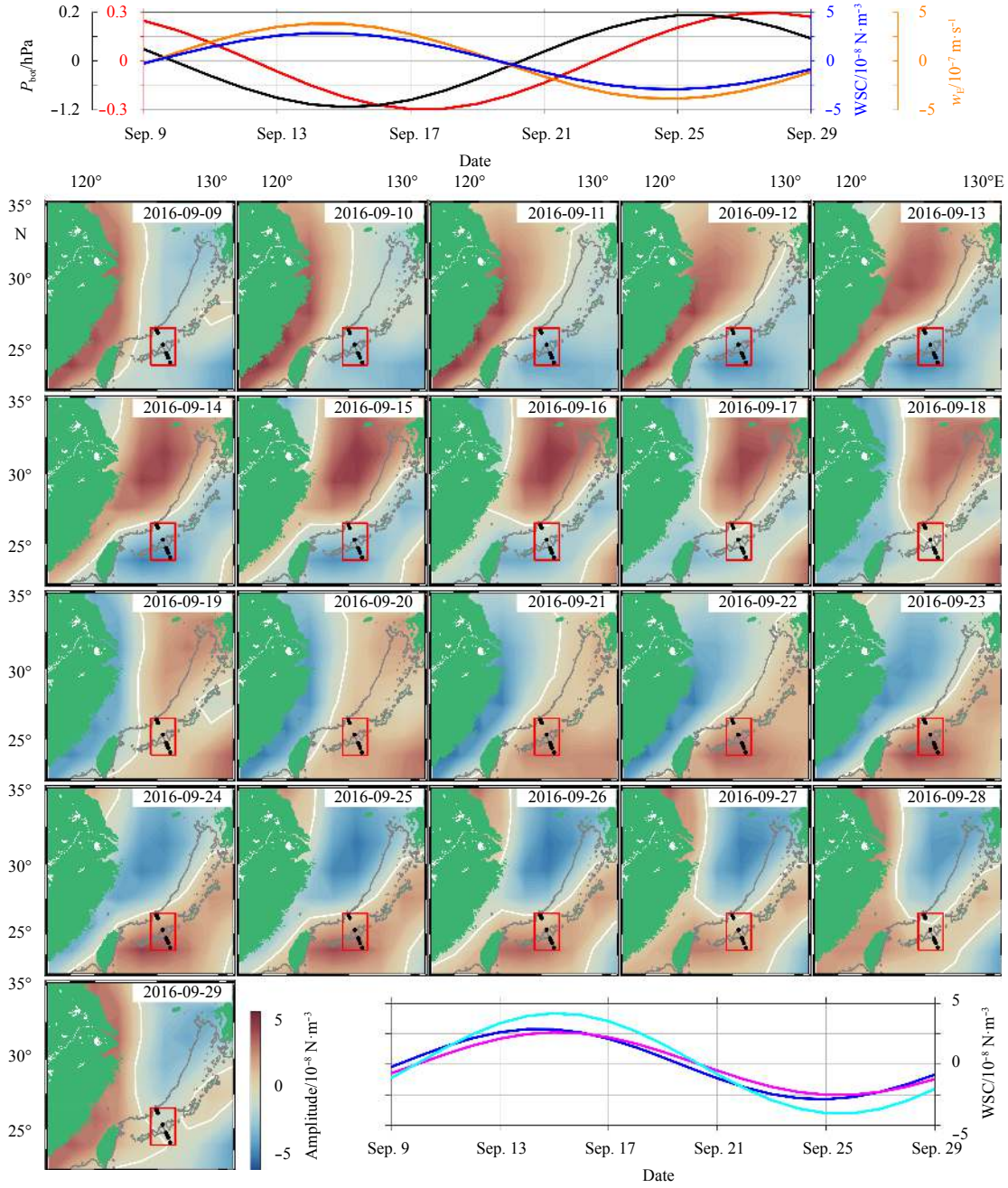

Fig. 8. Daily maps of band-pass-filtered (19.5–22.5 d) wind stress curl (WSC) from 9–29 September 2016. Colors show the 21-day WSC and white lines are zero contours. Black dots indicate pressure-recording inverted echo sounder (PIES)/current and pressure-recording inverted echo sounder CPIES sites. Gray lines are 200-m isobaths on the continental shelf of the East China Sea. The upper panel shows the time series of the spatially averaged modelled P_{bot21} on the continental shelf (the black line) and around the moored array (the red line), band-pass-filtered WSC (the blue line) from 9–29 September 2016; the Ekman pumping/suction velocity (the orange line) on the continental shelf from the NCEP/NCAR dataset is also indicated. Band-pass-filtered WSC on the continental shelf from NCEP/NCAR (the blue line), ERA-interim (the magenta line), and JRA-55 (the cyan line) datasets are indicated in the lower right-hand panel.

ing 13–16 and 24–25 February, respectively (blue line in bottom right panel of Fig. 10), corresponding to the largest negative and positive signals of P_{bot21} (black line). However, the variability around the mooring sites almost disappeared (~0.1 hPa in model, red line), which is consistent with the measured records. The pattern of P_{bot21} is confined around the large 21-day WSC region on the shelf. It is worth noting that on the continental shelf, the 21-day WSC propagated southeastwards during both September 2016 (Fig. 8) and February 2016 (Fig. 10), but the largest amplitude of the 21-day WSC extended farther south in September 2016 (close to the moored array) than it did in February 2016 (far from the moored array). It leads to a result that significant P_{bot21} around the mooring sites only happened in September.

The CEOF analysis method was used to extract the space

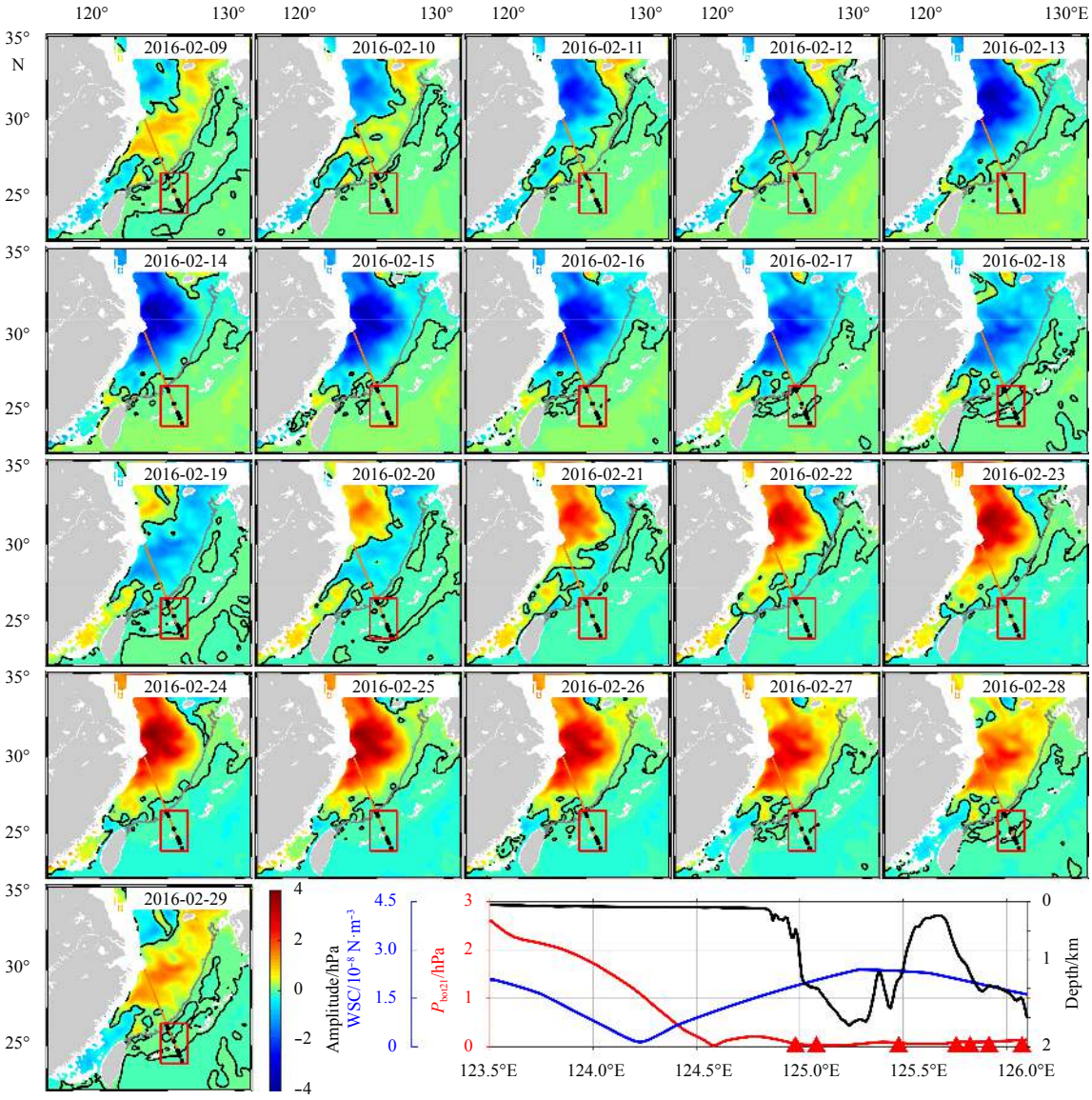

Fig. 9. Daily maps of modeled P_{bot21} and same as Fig. 7, but for 9–29 February 2016.

structure and phase during two periods (January to June 2016 and July to December 2016) based on the modeled P_{bot21}. Figure 11 shows the amplitude and phase patterns of CEOF results, since the first mode explained more than 90% of the variability for both periods (94.6% and 98.0%), only the first mode is shown here. It is easy to discern that the P_{bot21} mainly occurred on the continental shelf of the ECS and propagated southeastwards. During the period from January to June 2016, the amplitude was high east of the Changjiang Estuary and the dissipation was rapid on the southern ECS (Fig. 11a). The 21-day variability was fully dissipated and the phase was disordered when it extended to the Okinawa Trough (Figs 11a and b). During July to December 2016, a high-amplitude signal occurred in more southerly regions and extended to the moored array (Fig. 11c). According to the distribution of the phase, especially in Fig. 11d, the propagation velocity was slower in the shallow region close to coastline but increased on the continental shelf, corresponding to the velocity of the 21-day WSC in Fig. 8. The zero line in Fig. 8 moved slowly from 16 to 19 September 2016 and rapidly from 20 to 23 September 2016.

According to Na et al. (2016), the WSC dominates oceanic barotropic variability for short periods (7–15 days) and its effect remains important for periods of 15–30 days. Previous observations have indicated that local WSCs can influence the variability of P_{bot} with short periods (< 7–10 days) in the North Pacific. Non-local WSCs can be important for periods longer than 10 days (Luther et al., 1990; Na et al., 2012; Niiler et al., 1993). Our results show that the P_{bot21} observed by seven PIESs/CPIESs was associated with the P_{bot21} variability on the continental shelf of the ECS after being driven there by coastal WSCs; in contrast, the strong 21-day WSC around the mooring sites (Fig. 4e) could not induce such variability. To analyze the reasons for the 21-day WSC being able to induce such variability only in some areas, the governing barotropic vorticity equation for intraseasonal variability (Fu, 2003) was used:

$$\frac{\partial}{\partial t}\left(\nabla^2\xi - \frac{f^2}{gH}\xi\right) + HJ\left(\xi, \frac{f}{H}\right) = \frac{f}{\rho g}\vec{k}\cdot\nabla\times\left(\frac{\vec{\tau}}{H}\right), \quad (4)$$

where H is the depth, g is the gravitational acceleration, J repres-

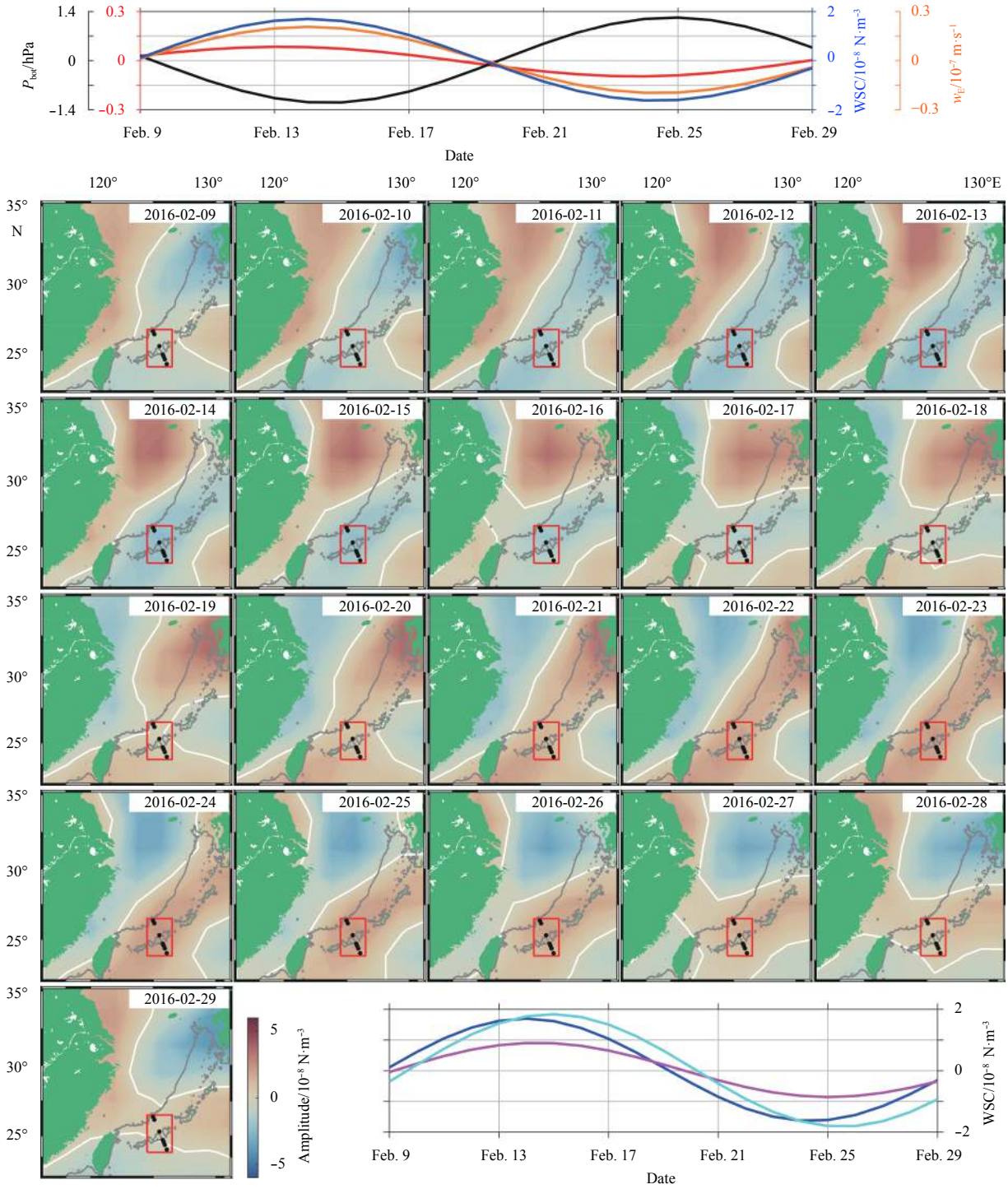

Fig. 10. Daily maps of band-pass-filtered (19.5–22.5 days) WSC and same as Fig. 8, but for 9–29 February 2016.

ents the Jacobian operator, and ξ is the sea level, which shows the same variability as the bottom pressure does in a one-layer barotropic model. In the model, $\left|\frac{\partial}{\partial t}\left(\nabla^2\xi\right)/\frac{\partial}{\partial t}\left(\frac{f^2}{gH}\xi\right)\right|$ was 10–1 000, indicating that $\frac{\partial}{\partial t}\left(\frac{f^2}{gH}\xi\right)$ could be neglected. Subsequently, the equation could be simplified as follows:

$$\frac{\partial}{\partial t}\left(\nabla^2\xi\right)+HJ\left(\xi,\frac{f}{H}\right)=\frac{f}{\rho g}\vec{k}\cdot\nabla\times\left(\frac{\vec{\tau}}{H}\right). \quad (5)$$

As shown in Fig. 12b, $R=\left|\frac{\partial}{\partial t}\left(\nabla^2\xi\right)/HJ\left(\xi,\frac{f}{H}\right)\right|$ decreased as the potential vorticity gradient indicated by $\sqrt{\left(\frac{\partial(f/h)}{\partial x}\right)^2+\left(\frac{\partial(f/h)}{\partial y}\right)^2}$ increased. $HJ\left(\xi,\frac{f}{H}\right)$ can be neglected at the region with a low potential vorticity gradient. Furthermore, $\sqrt{\left(\frac{\partial(f/h)}{\partial x}\right)^2+\left(\frac{\partial(f/h)}{\partial y}\right)^2}$ around the mooring array was ~10^{-13} m^{-2}·s^{-1} (Fig. 12a), corresponding to $R=4$. Therefore, Eq. (5) could be simplified as follows:

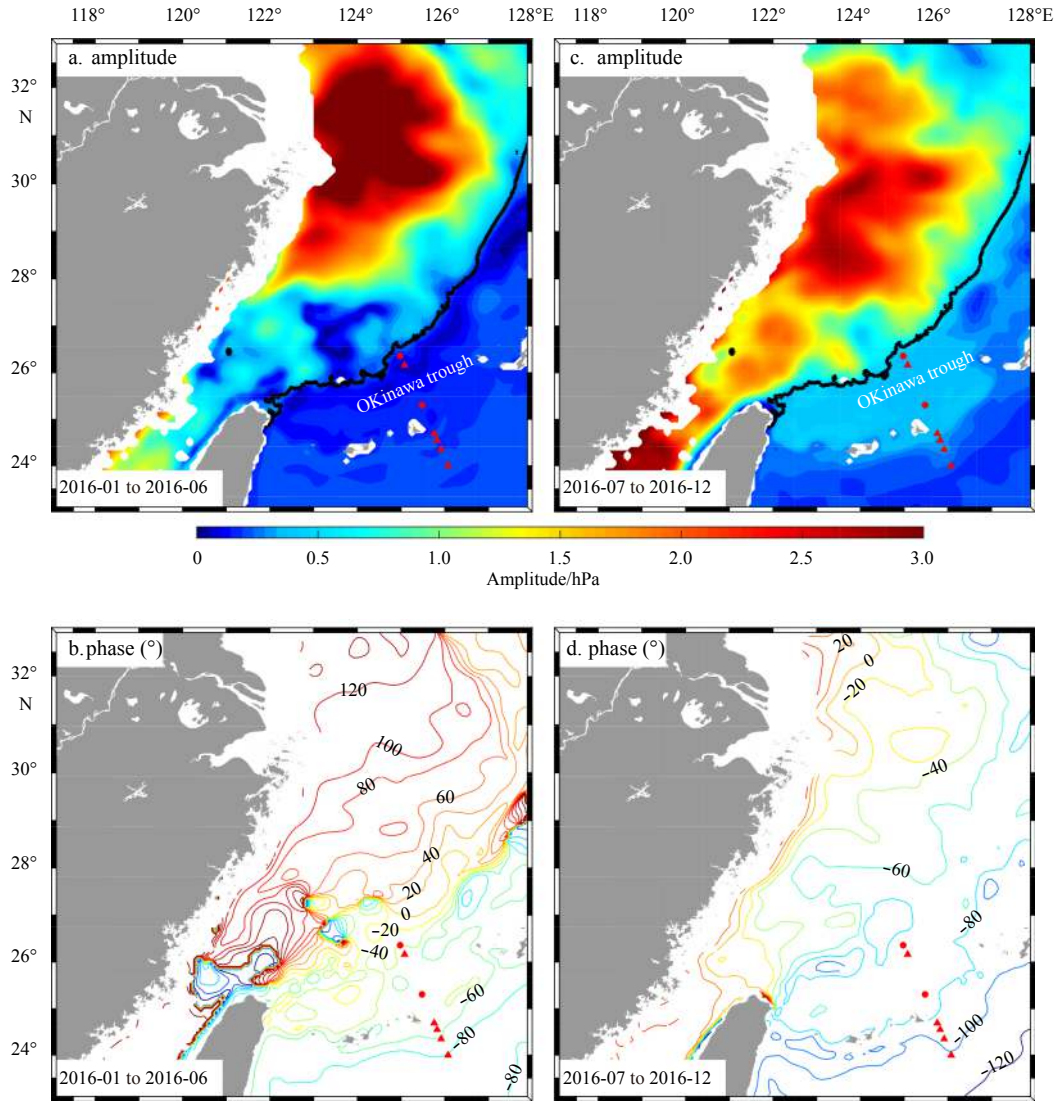

Fig. 11. Spatial patterns of amplitude (upper panels) and phase (lower panels) for the first mode of the complex empirical orthogonal function (CEOF) for the period January to June 2016 (a, b) and July to December 2016 (c, d) based on the modeled P_{bot21}. Locations of the pressure-recording inverted echo sounders (PIESs) (red dots) and current and pressure-recording inverted echo sounders (CPIESs) (red triangles) sites are also indicated. Black lines in a and c indicate the 200-m isobaths.

$$\frac{\partial}{\partial t}\left(\nabla^2\xi\right)=\frac{f}{\rho g}\vec{k}\cdot\nabla\times\left(\frac{\vec{\tau}}{H}\right). \tag{6}$$

Experiments with a flat bottom over the ECS at depths of 50, 100, 300, 500, 700, and 1 000 m were run during 2016 to determine the effect of depth on P_{bot21}. For a flat bottom model, $HJ\left(\xi,\frac{f}{H}\right)$ could be neglected as well. Moreover, $\frac{\partial}{\partial t}\left(\nabla^2\xi\right)$ was ~10^{-18} $\mathrm{m^{-1}\cdot s^{-1}}$ and ~10^{-19} $\mathrm{m^{-1}\cdot s^{-1}}$ at flat bottom depths of 100 and 1 000 m in the ECS, respectively, in both the modeled and wind-calculated results from 9–29 September 2016. The amplitude of P_{bot21} during this period decreased as the depth increased (Fig. 12c). Thus, the wind-driven P_{bot21} was much less significant in the deep region.

The amplitude from a real-depth model (Fig. 12c) was much lower than that from the fitted line, and $\frac{\partial}{\partial t}\left(\nabla^2\xi\right)$ was therefore not the only dominant factor in the ECS. The potential vorticity gradient in the ECS was much higher than that around the mooring array (Fig. 12a). In the ECS, R = 1, which indicated that $HJ\left(\xi,\frac{f}{H}\right)$ could not be neglected and that the topographic Sverdrup transport was important. Net "squashing/stretching" of the water columns occurred below the Ekman layer due to the downward/upward Ekman velocity. The squashing/stretching required a decrease/increase in potential vorticity, which was characterized by the advection of water columns across potential vorticity contours below the Ekman layer. The vorticity imparted to the ocean by the atmosphere through Ekman pumping/suction was compensated for by the advection of water columns across barotropic vorticity contours below the Ekman layer (Niiler and Koblinsky, 1985).

However, past wind forcing cannot have an infinite effect on the ocean. The P_{bot21} measured by PIESs/CPIESs propagated from the continental shelf and dissipated within days owing to the bottom friction. The response P_{bot} was related to forcing T through a simple forcing–response model, and the effect of bottom friction was considered as a damping time scale t (Wearn

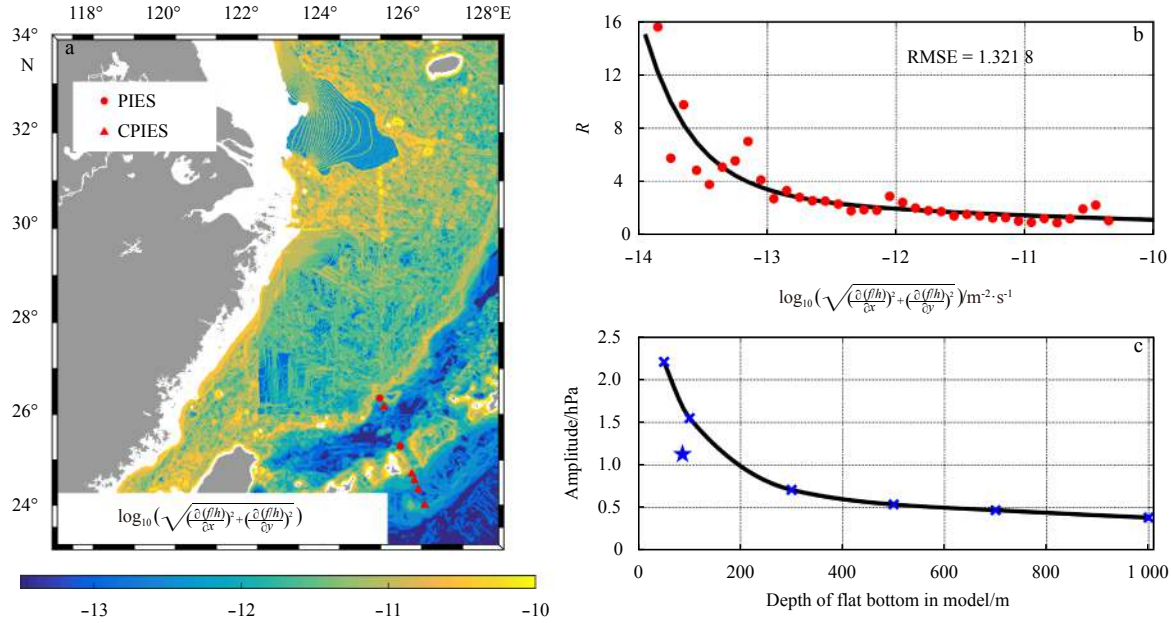

Fig. 12. Influence of topography. a. Distribution of potential vorticity gradient around the study region. Potential vorticity gradient is indicated by $\log_{10}\sqrt{\left(\frac{\partial(f/h)}{\partial x}\right)^2+\left(\frac{\partial(f/h)}{\partial y}\right)^2}$ here. b. Relationship of $R=\left|\frac{\partial}{\partial t}\left(\nabla^2\xi\right)/HJ\left(\xi,\frac{f}{H}\right)\right|$ versus potential vorticity gradient. Red dots are mean values of R in binsize of 0.1. c. Relationship of spatially averaged P_{bot21} amplitude (9–29 September 2016) on the continental shelf versus depth of flat bottom over the East China Sea. Blue crosses are cases calculated in model with depths of 50, 100, 300, 500, 700, and 1 000 m. Blue star indicates averaged amplitude and depth on the continental shelf from real-depth model.

and Baker, 1980):

$$\frac{\mathrm{d}P_{\mathrm{bot}}}{\mathrm{d}t}=T-\frac{P_{\mathrm{bot}}}{t}. \tag{7}$$

In Fourier space, t was calculated as follows (Fu, 2003; Weijer and Gille, 2005):

$$t=\frac{\tan\varphi}{\omega}, \tag{8}$$

where ω is angular frequency, and φ is the phase between P_{bot} and T. In the ECS, the 21-day WSC series lead P_{bot21} series approximately 10° ($t=$ 0.6 d) in the model, indicating that the effect of the past wind forcing was limited to ~0.6 days in the ECS.

Fu (2003) calculated t in another way:

$$t=\frac{H}{h_e f}, \tag{9}$$

where h_e is the thickness of the bottom frictional boundary layer, and H is the ocean depth. For h_e = 20 m (Armi and D'Asaro, 1980) and H = 86 m (averaged depth on the continental shelf), t was ~0.7 days in the ECS, slightly higher than that from the simple forcing–response model. P_{bot21} was significant in the shallow ocean under the strong 21-day WSC but dissipated rapidly on the shelf after leaving the strong 21-day WSC region. The signal that developed on the northern continental shelf in February did not reach the moored array because of the dissipation in the southern ECS (east of ~124°E in the lower panel of Fig. 9). The damping time scale was much longer in deeper regions according to Eq. (9). Thus, the dissipation was much slower there, as shown in the lower panel of Fig. 7.

4 Summary

We identified a 21-day P_{bot} response to the WSC on the continental shelf of the ECS based on PIESs/CPIESs measurements. The 21-day signal showed high amplitudes from July to December 2016 and propagated from KES1 to RES4 at ~2.4 m/s. According to the ROMS results, the spatial pattern of P_{bot21} on the continental shelf was consistent with the local 21-day WSC (Fig. 7–10), suggesting that the coastal WSC in the ECS induced the local P_{bot21}. P_{bot21} was generated from the coastline to the southeast in the ECS, following the propagation of the 21-day WSC that is perpendicular to the coastline. P_{bot21} continued to extend southeastward to the RIC with rapid dissipation after leaving the strong 21-day WSC region on the continental shelf. In contrast, although the signal measured by the mooring sites showed no coherence with the local WSC, it showed coherence with the WSC on the continental shelf; this indicates that P_{bot21} near the RIC was from the continental shelf. The strong 21-day WSC spatial pattern on the continental shelf extended further south in September than it did in February, which resulted in a southward shift of the high amplitude P_{bot21} region. The P_{bot21} was limited to the nearby areas of the 21-day WSC region, and P_{bot21} northeast of the Changjiang Estuary had dissipated on the shelf even before reaching the mooring sites in early 2016. Overall, the coastal ocean WSC could induce significant P_{bot21} on the broad continental shelf, while the deep ocean WSC could not.

The 21-day variability in the atmosphere is a widely existing phenomenon around the Yangtze Estuary and even across East Asia. For example, previous studies identified rainfall with periods including 21 days driven by wind in this region (e.g., Chen et

al., 2000; Mao and Wu, 2006; Yang et al., 2010). Our study shows the relationship between such common phenomena in atmospheric and oceanic variabilities. P_{bot21} in the ECS was driven by the coastal WSC through Ekman divergence/convergence; and then propagated southeastward towards the RIC following the propagation of 21-day WSC. Such 21-day WSC has occurred widely in history according to historical wind data, which suggests that the 21-day bottom pressure variability is not occasional but might be a widely existing phenomenon in this region. However, to date few studies have identified this signal owing to data sparsity, more observations are needed for further study.

Acknowledgements

In the deployment and recovery of instruments, we acknowledge the support and assistance of the captain, crew, scientists, supporting staff, and technicians aboard the T/V *Kagoshima-maru* of Kagoshima University.

References

Armi L, D'Asaro E. 1980. Flow structures of the benthic ocean. Journal of Geophysical Research: Oceans, 85(C1): 469–484, doi: 10.1029/jc085ic01p00469

Barnett T P. 1984. Interaction of the monsoon and Pacific trade wind system at interannual time scales. Part II: The tropical band. Monthly Weather Review, 112(12): 2380–2387, doi: 10.1175/1520-0493(1984)112<2380:IOTMAP>2.0.CO;2

Brown W, Munk W, Snodgrass F, et al. 1975. Mode bottom experiment. Journal of Physical Oceanography, 5(5): 75–85, doi: 10.1175/1520-0485(1975)005<0075:MBE>2.0.CO;2

Carrère L, Lyard F. 2003. Modeling the barotropic response of the global ocean to atmospheric wind and pressure forcing—Comparisons with observations. Geophysical Research Letters, 30(6): 1275, doi: 10.1029/2002GL016473

Chen T C, Yen M C, Weng Shuping. 2000. Interaction between the summer monsoons in East Asia and the South China Sea: Intraseasonal monsoon modes. Journal of the Atmospheric Sciences, 57(9): 1373–1392, doi: 10.1175/1520-0469(2000)057<1373:IBTSMI>2.0.CO;2

Flather R A. 1976. A tidal model of the northwest European continental shelf. Memoires de la Societe Royale des Sciences de Liege, 6(10): 141–164

Fu L L. 2003. Wind-forced intraseasonal sea level variability of the extratropical oceans. Journal of Physical Oceanography, 33(2): 436–449, doi: 10.1175/1520-0485(2003)033<0436:WFISLV>2.0.CO;2

Fu L L, Davidson R A. 1995. A note on the barotropic response of sea level to time-dependent wind forcing. Journal of Geophysical Research: Oceans, 100(C12): 24955–24963, doi: 10.1029/95JC02259

Fukumori I, Raghunath R, Fu L L. 1998. Nature of global large-scale sea level variability in relation to atmospheric forcing: A modeling study. Journal of Geophysical Research: Oceans, 103(C3): 5493–5512, doi: 10.1029/97jc02907

Gille S T, Hughes C W. 2001. Aliasing of high-frequency variability by altimetry: Evaluation from bottom pressure recorders. Geophysical Research Letters, 28(9): 1755–1758, doi: 10.1029/2000GL012244

Gilman D L, Fuglister F J, Mitchell Jr M J. 1963. On the power spectrum of "red noise". Journal of the Atmospheric Sciences, 20(2): 182–184, doi: 10.1175/1520-0469(1963)020<0182:OTPSON>2.0.CO;2

Hirose N, Fukumori I, Zlotnicki V, et al. 2001. Modeling the high-frequency barotropic response of the ocean to atmospheric disturbances: Sensitivity to forcing, topography, and friction. Journal of Geophysical Research: Oceans, 106(C12): 30987–30995, doi: 10.1029/2000jc000763

Jeon C, Park J H, Nakamura H, et al. 2019. Poleward-propagating near-inertial waves enabled by the western boundary current. Scientific Reports, 9(1): 9955, doi: 10.1038/s41598-019-46364-9

Kalnay E, Kanamitsu M, Kistler R, et al. 1996. The NCEP/NCAR 40-year reanalysis project. Bulletin of the American Meteorological Society, 77(3): 437–472, doi: 10.1175/1520-0477(1996)077<0437:TNYRP>2.0.CO;2

Kennelly M A, Tracey K L, Watts D R. 2007. Inverted echo sounder data processing manual, GSO Tech Rep, 2007–02. Narragansett: University of Rhode Island

Luther D S, Chave A D, Filloux J H, et al. 1990. Evidence for local and nonlocal barotropic responses to atmospheric forcing during BEMPEX. Geophysical Research Letters, 17(7): 949–952, doi: 10.1029/GL017i007p00949

Mao Jiangyu, Wu Guoxiong. 2006. Intraseasonal variations of the Yangtze rainfall and its related atmospheric circulation features during the 1991 summer. Climate Dynamics, 27(7–8): 815–830, doi: 10.1007/s00382-006-0164-2

Mathers E L, Woodworth P L. 2004. A study of departures from the inverse-barometer response of sea level to air-pressure forcing at a period of 5 days. Quarterly Journal of the Royal Meteorological Society, 130(597): 725–738, doi: 10.1256/QJ.03.46

Na H, Park J H, Watts D R, et al. 2012. Near 13 day barotropic ocean response to the atmospheric forcing in the North Pacific. Journal of Geophysical Research: Oceans, 117(C12): C12019, doi: 10.1029/2012JC008211

Na H, Watts D R, Park J H, et al. 2016. Bottom pressure variability in the Kuroshio Extension driven by the atmosphere and ocean instabilities. Journal of Geophysical Research: Oceans, 121(8): 6507–6519, doi: 10.1002/2016JC012097

Niiler P P, Filloux J, Liu W T, et al. 1993. Wind-forced variability of the deep eastern North Pacific: Observations of seafloor pressure and abyssal currents. Journal of Geophysical Research: Oceans, 98(C12): 22589–22602, doi: 10.1029/93JC01288

Niiler P P, Koblinsky C J. 1985. A local time-dependent Sverdrup balance in the eastern North Pacific Ocean. Science, 229(4715): 754–756, doi: 10.1126/science.229.4715.754

Nitani H. 1972. Beginning of the Kuroshio. In: Stommel H, Yoshida K, eds. Physical Aspects of the Japan Current. Seattle: University of Washington, 129–164

Park J H, Watts D R. 2005. Response of the southwestern Japan/East Sea to atmospheric pressure. Deep Sea Research Part II: Topical Studies in Oceanography, 52(11–13): 1671–1683, doi: 10.1016/j.dsr2.2003.08.007

Park J H, Watts D R. 2006. Near 5-day nonisostatic response of the Atlantic Ocean to atmospheric surface pressure deduced from sub-surface and bottom pressure measurements. Geophysical Research Letters, 33(12): L12610, doi: 10.1029/2006GL026304

Park J H, Watts D R, Donohue K A, et al. 2008. A comparison of in situ bottom pressure array measurements with GRACE estimates in the Kuroshio Extension. Geophysical Research Letters, 35(17): L17601, doi: 10.1029/2008gl034778

Park J H, Watts D R, Donohue K A, et al. 2012. Comparisons of sea surface height variability observed by pressure-recording inverted echo sounders and satellite altimetry in the Kuroshio Extension. Journal of Oceanography, 68(3): 401–416, doi: 10.1007/s10872-012-0108-x

Ponte R M. 1994. Understanding the relation between wind- and pressure-driven sea level variability. Journal of Geophysical Research: Oceans, 99(C4): 8033–8039, doi: 10.1029/94JC00217

Ponte R M. 1997. Nonequilibrium response of the global ocean to the 5-day Rossby-Haurwitz wave in atmospheric surface pressure. Journal of Physical Oceanography, 27(10): 2158–2168, doi: 10.1175/1520-0485(0)027<2158:NROTGO>2.0.CO;2

Ponte R M, Quinn K J, Wunsch C, et al. 2007. A comparison of model and GRACE estimates of the large-scale seasonal cycle in ocean bottom pressure. Geophysical Research Letters, 34(9): L09603, doi: 10.1029/2007GL029599

Qiu Chunhua, Mao Huabin, Liu Hailong, et al. 2019. Deformation of a warm eddy in the northern South China Sea. Journal of Geophysical Research: Oceans, 124(8): 5551–5564, doi: 10.1029/2019JC015288

Quinn K J, Ponte R M. 2011. Estimating high frequency ocean bottom

pressure variability. Geophysical Research Letters, 38(8): L08611, doi: 10.1029/2010GL046537

Talley L D, Pickard G L, Emery W J, et al. 2011. Descriptive Physical Oceanography: An Introduction. 6th ed. London: Academic Press

Thomson R E, Emery W J. 2001. Data Analysis Methods in Physical Oceanography. London: Elsevier

Trenberth K E, Large W G, Olson J G. 1990. The mean annual cycle in global ocean wind stress. Journal of Physical Oceanography, 20(11): 1742–1760, doi: 10.1175/1520-0485(1990)020<1742:TMACIG>2.0.CO;2

Wang Min, Liu Zhaojun, Zhu Xiaohua, et al. 2019. Origin and formation of the Ryukyu Current revealed by HYCOM reanalysis. Acta Oceanologica Sinica, 38(11): 1–10, doi: 10.1007/s13131-018-1329-7

Wang Qiang, Wang Yinxia, Bo Hong, et al. 2011. Different roles of Ekman pumping in the west and east segments of the South China Sea Warm Current. Acta Oceanologica Sinica, 30(3): 1–13, doi: 10.1007/s13131-011-0113-8

Watts D R, Qian Xiaoshu, Tracey K L. 2001. Mapping abyssal current and pressure fields under the Meandering Gulf Stream. Journal of Atmospheric and Oceanic Technology, 18(6): 1052–1067, doi: 10.1175/1520-0426(2001)018<1052:MACAPF>2.0.CO;2

Wearn Jr R B, Baker Jr D J. 1980. Bottom pressure measurements across the Antarctic circumpolar current and their relation to the wind. Deep Sea Research Part A. Oceanographic Research Papers, 27(11): 875–888, doi: 10.1016/0198-0149(80)90001-1

Weijer W, Gille S T. 2005. Adjustment of the southern ocean to wind forcing on synoptic time scales. Journal of Physical Oceanography, 35(11): 2076–2089, doi: 10.1175/jpo2801.1

Yang Jing, Wang Bin, Wang Bin, et al. 2010. Biweekly and 21-30-day variations of the subtropical summer monsoon rainfall over the lower reach of the Yangtze River basin. Journal of Climate, 23(5): 1146–1159, doi: 10.1175/2009JCLI3005.1

Zhang Kun, Zhu Xiaohua, Zhao Ruixiang. 2018. Near 7-day response of ocean bottom pressure to atmospheric surface pressure and winds in the northern South China Sea. Deep Sea Research Part I: Oceanographic Research Papers, 132: 6–15, doi: 10.1016/j.dsr.2017.12.004

Zhao Ruixiang, Nakamura Hirohiko, Zhu Xiao-Hua, et al. 2020. Tempo-spatial variations of the Ryukyu current southeast of Miyakojima island determined from mooring observations. Scientific Reports, 10(1): doi: 10.1038/s41598-020-63836-5

Zhao Ruixiang, Zhu Xiaohua, Park J H. 2017. Near 5-day nonisostatic response to atmospheric surface pressure and coastal-trapped waves observed in the Northern South China Sea. Journal of Physical Oceanography, 47(9): 2291–2303, doi: 10.1175/JPO-D-17-0013.1

Zhu Xiaohua, Han I S, Park J H, et al. 2003. The Northeastward current southeast of Okinawa Island observed during November 2000 to August 2001. Geophysical Research Letters, 30(2): 1071, doi: 10.1029/2002GL015867